



A 10-fold decline in the deep Eastern Mediterranean thermohaline overturning circulation during the last interglacial period

Journal Article**Author(s):**

Andersen, Morten B.; Matthews, Alan; Vance, Derek; Bar-Matthews, Miryam; Archer, Corey ; De Souza, Gregory 

Publication date:

2018-12-01

Permanent link:

<https://doi.org/10.3929/ethz-b-000295746>

Rights / license:

[Creative Commons Attribution-NonCommercial-NoDerivatives 4.0 International](#)

Originally published in:

Earth and Planetary Science Letters 503, <https://doi.org/10.1016/j.epsl.2018.09.013>

1 **A 10-fold decline in the deep Eastern Mediterranean thermohaline**
2 **overturning circulation during the last interglacial period.**

3

4 **Authors:** M Andersen^{1,2*}, A. Matthews³, D. Vance², M. Bar-Matthews⁴, C Archer², G
5 de Souza²

6 *corresponding author: andersenm1@cardiff.ac.uk

7 ¹Cardiff University, School of Earth & Ocean Sciences, Park Place, Cardiff CF10
8 3AT, United Kingdom

9 ²ETH Zürich, Institute of Geochemistry and Petrology, Department of Earth Sciences,
10 Clausiusstrasse 25, 8092 Zurich, Switzerland

11 ³Institute of Earth Sciences, Hebrew University of Jerusalem, 91904 Jerusalem, Israel

12 ⁴Geological Survey of Israel, Jerusalem 95501, Israel

13

14 **Keywords:** Mediterranean, sapropels, uranium isotopes, molybdenum isotopes, last
15 interglacial

16

17 word count: ~6500

18 ©2018. This manuscript version is made available under the CC-BY-NC-ND 4.0

19 license

20

21

22 **Abstract**

23 Present-day Mediterranean deep-waters are well oxygenated, but the episodic
24 formation of organic-rich sediments (sapropels) indicates that this pattern was

25 frequently perturbed in the past. Both high export productivity and disruption of the
26 thermohaline circulation, leading to reduced deep-water ventilation, have been
27 proposed to account for sapropel deposition and anoxia. The last interglacial sapropel
28 S5 is considered one of the most strongly developed. Here, we apply the redox-sensitive
29 Mo and U (elemental and isotope) systems to quantify the intensity of anoxic deep-
30 water conditions in the Eastern Mediterranean Sea from ODP core 967 (2550 mbsl).
31 Both U and Mo show strong authigenic enrichment, coupled to progressive increase in
32 $\delta^{98}\text{Mo}_{\text{auth}}$ (1.2-1.8‰ to +2.0-2.3‰) and decrease in $\delta^{238}\text{U}_{\text{auth}}$ (+0.10‰ to -0.15‰) from
33 the beginning to the end of S5, suggesting increasing water column euxinia and removal
34 fluxes of Mo and U. Based on modern euxinic basins, we show that sedimentary
35 $\delta^{238}\text{U}_{\text{auth}}$ can be used to derive estimates of water column U depletion and, ultimately,
36 deep-water renewal rates. These principles are first tested on the modern Black Sea,
37 which yields calculated deep-water renewal times of $830^{+690}/_{-500}$ years, in good
38 agreement with independent estimates. Applying these principles to the end of S5
39 suggests bottom-water U depletion of ~50% and deep-water renewal times of $1030^{+820}/_{-520}$
40 years. The significantly slower deep-water renewal rates in the Eastern
41 Mediterranean Sea compared to today (~100 years) would have played an important
42 role in the formation of sapropel S5 and are consistent with the proposed suppression
43 of overturning during the last interglacial, due to increased stratification resulting from
44 higher riverine freshwater input under enhanced monsoon forcing.

45

46 **1. Introduction**

47 The Mediterranean overflow system and outflow into the Atlantic plays a major role in
48 Atlantic Meridional Overturning Circulation (AMOC) (Johnson and Stevens, 2000;
49 Rogerson et al., 2012). In its current configuration, the Mediterranean Sea is

50 characterized by large-scale thermohaline circulation in which the relatively low
51 salinity inflow from the Atlantic is converted via high evaporation in the Eastern
52 Mediterranean Basin into an intermediate-depth saline outflow (Levantine Intermediate
53 Water) (Malanotte-Rizzoli and Bergamasco, 1989; Pinardi and Masetti, 2000; Rohling
54 et al., 2015) (Fig. 1). Such a circulation pattern leads to the formation of well-
55 oxygenated deep-water in both the Eastern and Western Mediterranean basins,
56 separated by the straits of Sicily. In the past, however, the periodic formation of organic
57 carbon-rich sediments, termed sapropels, suggests that the redox state of deep-waters
58 changed (e.g, Rossignol Strick, 1985; Rohling and Hilgren, 1991; Emeis et al, 1998;
59 Emeis et al, 2000; Rohling et al., 2015).

60

61 Sapropels are associated with anoxic conditions in the deep ocean that allow the
62 preservation of organic matter. Both higher export productivity, creating anoxia
63 through enhanced consumption of oxygen, and disruption of oxygen supply via changes
64 in the thermohaline circulation, have been proposed to account for the formation and
65 preservation of organic matter (Rossignol-Strick, 1985; Rohling and Hilgen, 1991;
66 Emeis et al., 2000; de Lange et al., 2008; Meyer and Kump, 2008). Pleistocene
67 Mediterranean sapropels are unique sediments in that their periodicity is correlated with
68 high northern hemisphere summer insolation during minima in the *ca.* 21 ka orbital
69 precession cycle, and they are particularly well developed during interglacials. The
70 resultant organic carbon-rich sedimentary deposits are important and useful analogs for
71 such sediments in deeper time in Earth history. In this paper, we explore the validity of
72 disrupted thermohaline circulation as a forcing factor in the creation of anoxia.
73 Enhanced monsoon-driven freshwater runoff into the surface of the Eastern
74 Mediterranean, through the Nile or transient North African rivers, or both, have all been

75 put forward as important factors in the creation of less saline surface water layers. This,
76 in turn, may have led to partial stratification of the water body and disruption of the
77 thermohaline circulation system (Rossignol Strick et al., 1982; Emeis et al., 2000;
78 Osborne et al., 2008; Bar-Matthews, 2014; Rohling et al., 2015). It is also recognized
79 that some ‘preconditioning’ may have occurred, through the prior formation of anoxic
80 deep-waters due to enhanced regional rainfall and sea level rise following glacial
81 maxima (Grimm et al., 2015; Grant et al., 2016).

82

83 Geochemical proxies for redox conditions prevailing prior to and during sapropel
84 formation, and following their termination as oxic conditions returned, include: organic
85 biomarkers, elements sensitive to paleoproductivity and organic burial (e.g. barium)
86 and redox-sensitive trace elements (RSTE, e.g. iron, manganese, vanadium,
87 molybdenum, uranium) (Thomson et al., 1999; Cane et al., 2002; Rohling et al., 2006;
88 de Lange et al., 2008; Almogi-Labin et al., 2009; Gallego-Torres et al., 2010). For
89 instance, using a powerful combination of ^{14}C dating and RSTE profiles, de Lange et
90 al. (2008) showed that basin-wide anoxic conditions prevailed during the formation of
91 the latest (Holocene) sapropel, S1, at water depths > 1800m.

92

93 The stable isotope systems of the metals molybdenum and uranium, which
94 fractionate during oxidation-reduction processes, can record distinctive isotope
95 signatures during organic carbon-rich sedimentation (Barling et al., 2001; Arnold et al.,
96 2004; Neubert et al., 2008; Weyer et al., 2008; Nägler et al., 2011; Andersen et al., 2014).
97 In today’s oxic oceans, the isotope composition of dissolved Mo ($\delta^{98}\text{Mo} +2.34\text{‰}$,
98 reported in delta-notation as $\delta^{98}\text{Mo}$ using the $^{98}\text{Mo}/^{95}\text{Mo}$ ratio normalized to NIST SRM
99 3134 standard +0.25 in parts per thousand; Nägler et al., 2014), dominated by the

100 oxyanion molybdate species (MoO_4^{2-}), is thought to be fractionated relative to the Mo
101 input to the ocean ($\delta^{98}\text{Mo} \sim +0.7\text{‰}$; Archer & Vance 2008) mostly because of the loss
102 of Mo adsorbed to manganese oxides ($\delta^{98}\text{Mo} \sim -0.7\text{‰}$; Barling et al., 2001). In contrast,
103 strongly euxinic (anoxic+sulfidic) water conditions result in near-quantitative uptake
104 of Mo from seawater (either by scavenging to organic matter or through formation of a
105 colloidal Fe-Mo-S species; Helz et al., 2011), driven by the transformation of
106 molybdate to tetra-thiomolybdate (MoS_4^{2-}), with $\text{MoS}_4^{2-} \gg \text{MoO}_4^{2-}$ when
107 concentrations of H_2S are above $11 \mu\text{Mol}$ (e.g. Neubert et al. 2008). This leads to
108 organic carbon-rich sediments acquiring a $\delta^{98}\text{Mo}$ value very close to that of seawater,
109 as has been recognized in organic carbon-rich sediments deposited in the euxinic deep
110 Black Sea (Neubert et al., 2008; Nägler et al., 2011; Wegworth et al., 2018).
111 Intermittent or weaker (H_2S concentrations $<11 \mu\text{Mol}$) euxinic conditions, on the other
112 hand, may lead to isotopically lighter Mo in sediments due to isotope fractionation
113 during incomplete MoO_4^{2-} to MoS_4^{2-} transformation (Poulson-Brucker et al., 2012; Kerl
114 et al., 2017). In sub-oxic to anoxic conditions, Mo isotope signatures intermediate
115 between those of seawater and the oxic end-member may also reflect the importance of
116 adsorption of isotopically light Mo species on iron oxides and pyrite (Goldberg et al.,
117 2009). Indeed, $\delta^{98}\text{Mo}$ values much lower than modern seawater, and inferred weakly
118 euxinic to anoxic conditions, have been observed in middle Pleistocene sapropels and
119 in the most recent Holocene sapropel S1 at 2550 m water depth (Scheiderich et al.,
120 2011; Azrieli-Tal et al., 2014). $\delta^{98}\text{Mo}$ minima from seawater during the early diagenesis
121 of sapropel S1 in the Nile Fan have also been explained by Mo isotope fractionation
122 during the kinetically-controlled particulate uptake of porewater thiomolybdate species
123 (Matthews et al., 2017).

124

125 The mechanism for authigenic uranium enrichment in reduced sediments differs
126 from that of molybdenum: while Mo removal primarily occurs in a euxinic water
127 column, the major U uptake has been shown to, instead, occur within the reducing
128 sediment environment, mediated by metal- and sulfate-reducing bacteria (Anderson et
129 al., 1989; Lovley et al., 1991; McManus et al. 2006). The isotope system of the uranium
130 parents ($^{238}\text{U}/^{235}\text{U}$, given in typical delta-notation as $\delta^{238}\text{U}$, which is the parts per
131 thousand difference relative to the normalizing CRM-145 standard) has also been
132 shown to respond to redox state as a result of significant positive isotope fractionation
133 during the reduction of hydrated and complexed U(VI) ion to the largely immobile
134 U(IV) ion (Stirling et al., 2007; Weyer et al., 2008; Andersen et al., 2017). Weyer et al.
135 (2008) showed that $^{238}\text{U}/^{235}\text{U}$ from organic carbon-rich in Black Sea sediments was 0.4
136 to 0.8‰ higher than seawater, and subsequent studies have applied the $\delta^{238}\text{U}$ system as
137 a paleoproxy for oceanic anoxia in ancient marine sediments (e.g. Montoya-Pino et al.,
138 2010; Kendall et al, 2015). Andersen et al. (2014) showed that mass balance during the
139 diffusion of uranium species through seawater and porewater constrains the $\delta^{238}\text{U}$
140 values preserved in sediment. This and subsequent studies (e.g. Noordmann et al.,
141 2015; Holmden et al., 2016) have shown that mass-balance constraints at the sediment-
142 water interface can lead to variable observed U isotope compositions, and that only a
143 steady state situation involving U diffusion and uptake allows for quantitative
144 interpretations of the $\delta^{238}\text{U}$ values in organic carbon-rich sediments.

145

146 Given the different mechanisms by which Mo and U isotopes respond to different
147 redox situations, the combined isotope systematics of these elements offers enormous
148 potential for quantifying and modeling oceanic processes during the formation of
149 organic carbon-rich sediments, as recently demonstrated for the saline Lake Rogoznica,

150 Adriatic Sea, Croatia (Bura-Nakić et al., 2018) and other modern and ancient organic-
151 rich sediments (e.g. Kendall et al., 2015; Noordmann et al., 2015). Here we utilize
152 coupled Mo and U isotope and RSTE systematics to study the evolution of redox
153 conditions in the Eastern Mediterranean Sea during the formation of the last interglacial
154 sapropel S5 (Eemian) period. We present data for the elemental and isotopic systems
155 of Mo and U in sapropel S5 in a deep-water setting (2550m) with the ultimate aim of
156 understanding the intensity of euxinia in deep-waters and quantify related slowdown in
157 the thermohaline circulation of the Eastern Mediterranean Sea. Our study employs a
158 new methodology based on U isotopes that can potentially be applied to other settings
159 with density driven oceanic circulation. Thus, as part of the verification of the approach,
160 we derive robust deep-water renewal times for the modern Black Sea.

161

162 **2. Samples and setting**

163 An extensive review of the Mediterranean climate, oceanography and periodic
164 development of sapropels (particularly S1 and S5) is given by Rohling et al. (2015).
165 Sapropel S5 was deposited during the last interglacial insolation maximum. It is
166 considered to be the most intensely developed and most pristine of the more recent
167 sapropels in the Eastern Mediterranean, Aegean and Levantine basins, with anoxia and
168 euxinia extending up to as high as ~200 m below the sea surface (Rohling et al., 2006).
169 It differs from sapropel S1, for which anoxic conditions only existed at open water
170 depths of >1800m (deLange et al., 2008). In S1, Mo isotopes indicate that only weakly
171 euxinic conditions developed in bottom waters (ODP Core 967D, 2550m depth;
172 Azrieli-Tal et al., 2014). The samples of sapropel S5 (abbreviated “S5” in the
173 following) were taken from ODP core 967C, drilled at a water depth of 2550m south
174 of Cyprus, at the base of the northern slope of the Eratosthenes Seamount (Fig. 1). This

175 study uses the dried and sieved <63 μm fraction of the samples analysed by Scrivner et
176 al. (2004) for Nd isotope measurements in foraminifera (ODP 967C-H5, 70 to 110 cm),
177 covering S5 and depths immediately above and below. Previous studies using the <63
178 μm fraction indicate that they provide a representative record of the elemental and
179 isotope geochemistry of sapropels (Box et al., 2011; Azrieli-Tal et al., 2014). For core
180 967C-H5, benthic extinction occurs at 103 cm and benthic reoccurrence appears above
181 approx. 74.5 cm. The S5 interval is defined to be within these boundaries (Cane et al.,
182 2002). Total organic carbon (TOC) values determined for the same sample interval (by
183 Emeis et al., 1998) show enrichments consistent with these boundaries (Supplementary
184 Table), indicating that post-sapropel oxidation (oxidative burndown) did not
185 significantly affect S5 at this core site. A 4.5 cm hiatus in the middle of S5 was proposed
186 by Cane et al. (2002), terminating at 87 cm. By correlation to the Soreq cave $\delta^{18}\text{O}$
187 record, (Bar-Matthews et al., 2000) the S5 interval has been dated to 128-120 ka
188 (Rohling et al., 2015).

189

190 **3. Methods**

191 Sample preparation and measurements were conducted at the facilities of the Bristol
192 Isotope Group, University of Bristol, United Kingdom (U and Mo isotopes; clean
193 laboratory chromatographic U separation), Hebrew University, Israel (clean laboratory
194 chromatographic Mo separation), and Geological Survey of Israel (trace and major
195 element chemistry).

196

197 *3.1 Major and trace metal chemistry and analyses*

198 Sample digestion for Mo separation and isotopic analysis was done in the clean
199 laboratory at the Hebrew University of Jerusalem (HUJ). Samples were pyrolyzed at

200 800°C for approximately 12 hours to oxidize organic carbon. The pyrolyzed residue was
201 then dissolved using HF, HNO₃ and HCl in the presence of H₂O₂. Trace and major
202 element concentrations of 13 sediment samples were measured by low temperature
203 plasma ashing of weighed amounts of sediments, followed by sodium peroxide
204 sintering and chemical analysis at the Geological Survey of Israel using ICP-OES for
205 major (Perkin Elmer Optima 3300) and ICP-MS for trace elements. Six samples were
206 analyzed after pyrolysis and digestion by ICP-MS at HUJ. Based on the analysis of two
207 geostandards (BHVO-1 and GIT-IWG IF-6) analytical errors (RSD) on single values
208 for major and trace elements were within ±5%.

209

210 *3.2 Molybdenum preparation and isotope analyses*

211 Molybdenum separation for isotopic analysis was done using the procedure of Archer
212 and Vance (2008), which sequentially elutes matrix elements, Cu, Fe and Mo. Prior to
213 column chemistry, 1 ml of pre-cleaned anion exchange resin (Biorad anion resin AG
214 MP-1 m, 100-200 mesh, chloride form) was loaded into 10 ml plastic Muromac[®]
215 columns. The resin was then pretreated with 0.05M HNO₃, followed by 7M HCl
216 containing 0.01% of 30% H₂O₂. Following elution, solutions were centrifuged to
217 remove any particle contaminants, fluxed three times with 0.5 ml 15M HNO₃ and dried.

218

219 Molybdenum isotopic analyses were carried out at the University of Bristol, using
220 a ThermoQuest Neptune instrument at low mass resolution ($M/\Delta M \sim 500$). Solutions
221 were introduced into the mass spectrometer in a 2% (v/v) HNO₃ solution by means of
222 a CPI (Amsterdam, The Netherlands) PFA nebulizer and spray chamber fitted to a
223 CETAC Aridus. Mass discrimination correction was achieved using a double spike, as
224 described previously by others for Mo (Siebert et al., 2001) and using the specific

225 procedure previously described for Zn (Bermin et al., 2006). All mass spectrometric
226 errors were propagated through the double-spike calculation to obtain the final
227 analytical uncertainty. Details of standards, calibration procedures, and error treatments
228 are given in Azrieli-Tal et al. (2014). Replicate analyses of a multi-element standard
229 (Me: Merck VI, 30 elements) run through the complete solution chemistry gave $\delta^{98}\text{Mo}$
230 = $-0.03 \pm 0.15\text{‰}$ (2SD). All Mo isotope compositions for samples are corrected from
231 the working CPI Mo ICPMS standard at Bristol ($\delta^{98}\text{Mo}$ Pacific Sea water = $2.26 \pm$
232 0.03‰ (2SD); Archer and Vance, 2008) to the recommended NIST SRM 3134 $\delta^{98}\text{Mo}$
233 = -0.25‰ (giving a $\delta^{98}\text{Mo}$ of 2.34‰ for seawater) (Nägler et al., 2014).

234

235 *3.3 Uranium preparation and isotope analysis*

236 Samples (10-50 mg) were dissolved in steps involving concentrated HNO_3 , HF, HCl
237 and H_2O_2 . At the first dissolution step, in HNO_3 and HF, the IRMM3636 $^{236}\text{U}/^{233}\text{U}$
238 double spike was added, aiming for a $^{236}\text{U}/^{235}\text{U}$ of ~ 4 . After heating, fluxing and
239 subsequent drying, steps using heated 6 M HCl (x2) and a 7 M HNO_3 + 30% H_2O_2
240 mixture were completed, before samples were re-dissolved in 10 ml of 3 M HNO_3 in
241 preparation for U-Teva chromatographic chemistry, following protocols in Andersen et
242 al. (2014). Purified U fractions were dried and prepared for mass spectrometry in 2%
243 (v/v) HCl aiming for 100-200 ppb U. Full procedural chemistry blanks were < 20 pg U.

244

245 Uranium isotopic analyses were carried out at the University of Bristol, using a
246 ThermoQuest Neptune instrument at low mass resolution ($M/\Delta M \sim 500$) by means of a
247 CPI (Amsterdam, The Netherlands) PFA nebulizer and spray chamber fitted to a
248 CETAC Aridus. The set-up and measurement protocols were as outlined in Andersen
249 et al. (2014; 2015). In brief, all Faraday cups were equipped with $10^{11} \Omega$ resistors, apart

250 from the cup for ^{238}U ($10^{10}\ \Omega$). Measurements were conducted with “standard” sampler
251 and “X” type skimmer cones. Typical sample ion beam intensities were $\sim 1\ \text{nA}$ for ^{238}U
252 using $\sim 50\ \text{ng U}$ per analysis. Measurements of two unknowns were bracketed with the
253 CRM-145 uranium standard, spiked in similar fashion as the unknowns. The in-house
254 CZ-1 uraninite standard, processed through U-Teva chemistry and periodically
255 measured in a similar fashion to the sediment samples, yielded $\delta^{238}\text{U}$ of -0.055 ± 0.032
256 ($\pm 2\text{S.D.}$) for ten repeats, in excellent agreement with previously published
257 compositions for this standard (Stirling et al., 2007; Andersen et al., 2015). The external
258 reproducibility for the CZ-1 standard is used as the uncertainty estimate for each of the
259 unknowns.

260

261 **4. Results**

262 *4.1 Sediment geochemistry*

263 Several geochemical parameters allow the distinction of the S5 horizon from the
264 sediments just above and below (Fig. 2, Table 1 and Supplementary Table). Both [TOC]
265 ($>2\%$) and [Ba] (2500-700 ppm) are higher during S5 than the surrounding sediments
266 ([TOC] $<1\%$, [Ba] 180-550 ppm). Concentrations of the RSTE [U] (13-37 ppm), [Mo]
267 (25-140 ppm) and [V] (397-194 ppm) are highly elevated within S5, whereas the
268 surrounding sediments have moderately elevated [U] (5-9 ppm), [Mo] (2-6 ppm) and
269 [V] (166-74 ppm) compared to typical detrital background concentrations. The
270 sediments surrounding S5 have $\delta^{98}\text{Mo}$ values ranging from $+1.2$ to $+2.0\text{‰}$, while within
271 S5, $\delta^{98}\text{Mo}$ increases systematically from $+1.0$ - $+1.8\text{‰}$ in the lower sections (102 to 90
272 cm) to $+1.9$ - $+2.3\text{‰}$ in the upper sections (90 to 76 cm). The $\delta^{238}\text{U}$ compositions range
273 from -0.35 to -0.22‰ in the sediments above and below the sapropel, while within S5,
274 $\delta^{238}\text{U}$ values decrease systematically from approx. $+0.10\text{‰}$ in the lower sections (102

275 to 94 cm) to approx. -0.15‰ in the upper sections (94 to 76 cm). Normalizing [Fe],
276 [U], [Mo] and [V] to [Al], a typical refractory element, reveals similar behavior to that
277 of the absolute concentrations alone, with more elevated ratios during S5 than in the
278 surrounding sediments, particularly in the later part of S5 (Fig. 3).

279

280 *4.2 Authigenic Mo and U estimates in the sediments*

281 A common method for estimating the authigenic fraction uses the measured [U] and
282 [Mo] compared to [Al] (e.g. Algeo & Tribovillard, 2009), and normalizes these ratios
283 to the estimates from detrital terrigenous siliciclastics, giving relative authigenic
284 enrichment factors (EF) for U and Mo. Such EF estimates (see Table 1 for detrital
285 Mo/Al and U/Al compositions used) suggest that the authigenic fraction dominates both
286 the Mo and U budget during S5 (>94%) and that it also contributes a significant fraction
287 in the surrounding sediments (72-93%). These values correspond to EFs of 21-101 for
288 U (U_{EF}) and 35-327 for Mo (Mo_{EF}) during S5, and 4-16 for both in the surrounding
289 sediments (Supplementary Table). The sediments surrounding S5 have relatively
290 higher U_{EF} compared to the corresponding Mo_{EF} , while the Mo_{EF}/U_{EF} ratios towards
291 the end of S5 are close to the present-day seawater Mo/U ratio. Comparing the
292 sediments to the schematic marine water mass trajectories from physical and chemical
293 controls on water masses of Algeo & Tribovillard (2009), they broadly follow a
294 trajectory implying progression through open marine anoxic-sulfidic conditions
295 (elevated Mo_{EF} over U_{EF}), although the sediments at the end S5 deviate from this trend
296 and plot close to the Mo/U seawater ratio. There is a clear difference between the Mo_{EF}
297 to U_{EF} trends in S5 compared to trajectories seen in Black Sea sediments (Algeo &
298 Tribovillard 2009). The latter show a flatter trajectory (high enrichment factors with

299 elevated U_{EF} over Mo_{EF}) that reflects Mo depletion in a highly restricted basin (see Fig
300 4a).

301

302 Authigenic U can furthermore be considered to belong to two main fractions: U from
303 biogenic carbonates (which have low [Mo] and are not important for this element) and
304 U incorporated from *in situ* uranium reduction within the sediments. Following
305 procedures in Andersen et al. (2014), which assume that the [Ca] in bulk sediments is
306 primarily from biogenic carbonates with ~1 ppm U content, the relative U contribution
307 from this carbonate source to the authigenic fraction may also be estimated. This
308 calculation shows that the biogenic carbonate U fraction constitutes <1% for S5 and
309 <5% for surrounding sediments (Supplementary Table), so that the vast majority of U
310 in these sediments is due to *in situ* reduction.

311

312 The isotope composition of the authigenic Mo and U fractions can also be
313 estimated using the elemental concentrations in combination with Mo and U isotope
314 compositions for the detrital terrigenous siliciclastic and (for U only) biogenic
315 carbonate fractions. Here, values of $\delta^{238}U = -0.3\text{‰}$ and $\delta^{98}Mo = 0\text{‰}$ were used for the
316 detrital terrigenous sediments and $\delta^{238}U = -0.4\text{‰}$ for biogenic carbonate (Andersen et
317 al. 2017; Kendall et al. 2017). Uncertainties on the authigenic composition were
318 propagated by weighting the relative size of the detrital component following Andersen
319 et al. (2014), see Table 1 for details. The dominance of the authigenic fraction for Mo
320 and U generally leads to insignificant changes between the measured bulk and
321 estimated authigenic $\delta^{238}U$ and $\delta^{98}Mo$ (Table 1). The only significant changes are for
322 $\delta^{98}Mo_{auth}$ values from the sediments surrounding S5 (from +0.14 to +0.65‰ higher for
323 $\delta^{98}Mo_{auth}$). Thus, whereas the bulk sediment $\delta^{98}Mo$ values of +1.4 to +2.1‰ broadly

324 bracket the typical value of +1.6‰ in anoxic continental margin marine sediments
325 (Poulson-Brucker et al., 2009), $\delta^{98}\text{Mo}_{\text{auth}}$ values (+1.6 to +2.4‰) shift toward the
326 seawater $\delta^{98}\text{Mo}$ composition.

327

328 **5. Discussion**

329 All the measured sediments show signs of being deposited under oxygen-poor
330 conditions (Figures 2 to 4). In the following, the sediments above and below S5 will be
331 discussed first, before turning to the S5 sediments themselves, and how these results
332 may be interpreted in terms of water column anoxia and deep-water renewal rates.

333

334 *5.1 Mo and U uptake in the sediments surrounding S5*

335 The sediments surrounding S5 are characterized by moderate U and Mo enrichment
336 factors typical for an anoxic marine setting, accumulating relatively more authigenic U
337 than Mo (see Fig. 4a). The observation of sediment anoxia prior to S5 fits well with
338 previous suggestions of anoxia developing ~3000 year earlier than the actual S5
339 (Schmiedl et al., 2003), likely due to gradual Mediterranean surface water freshening
340 associated with global sea-level rise (Rohling et al., 2015; Grant et al., 2016). The
341 termination of S5 somewhere between sediments at 77 and 72 cm is distinctive and
342 sharp for all proxies (Figures 2 and 3) and coincides with that indicated by [TOC] and
343 [Ba], suggesting no significant post-depositional oxidative burn-down.

344

345 Both $\delta^{98}\text{Mo}_{\text{auth}}$ (+1.6 to +2.4‰) and $\delta^{238}\text{U}_{\text{auth}}$ (-0.35‰ to -0.17‰) in the
346 sediments surrounding S5 are close to modern seawater values (+2.34‰ for $\delta^{98}\text{Mo}$ and
347 -0.39‰ for $\delta^{238}\text{U}$). Authigenic $\delta^{238}\text{U}$ compositions near the seawater value have been
348 observed in organic carbon-rich sediments from settings with periodically anoxic deep

349 waters, presumably due to non-steady state diffusive U transport into, and removal
350 within, sediments (e.g. Weyer et al., 2008; Andersen et al., 2014; Noordmann et al.,
351 2015; Andersen et al., 2017). In such a setting, however, the $\delta^{98}\text{Mo}$ would be expected
352 to be lower than the seawater composition, due to partial conversion of MoO_4^{2-} to
353 MoS_4^{2-} under anoxic and possibly weakly euxinic water column conditions (e.g. Azriel-
354 Tal et al., 2014). Instead, the Mo and U isotope compositions suggest near quantitative
355 uptake of both authigenic U and Mo, but with relatively moderate U and Mo enrichment
356 factors (Fig 4). This observation might suggest that uptake of authigenic Mo, as well as
357 U, mainly occurs from pore-waters within the sediment. Uranium and Mo supply to
358 these reducing porewaters is then limited by diffusion through a non-sulfidic
359 penetration zone with finite depth, which leads to near-quantitative uptake for U and
360 Mo at depths where pore-water sulfide concentrations are elevated enough to allow *in*
361 *situ* precipitation of sulfide minerals like pyrite. The latter proposition could be
362 supported by the relatively high sulfur content of all the sediments surrounding S5 (0.3
363 to 1.1 wt%; Supplementary Table). It should be noted that the highest $\delta^{98}\text{Mo}_{\text{auth}}$ values
364 (those closest to seawater composition) in the non-sapropel sediments, are for the pre-
365 sapropel samples. In contrast, post-sapropel sediments have slightly lower $\delta^{98}\text{Mo}_{\text{auth}}$
366 values (1.6 to 1.9‰), which may reflect incomplete Mo uptake from porewaters.

367

368 *5.2 Molybdenum and U uptake in sediments within S5*

369 Within S5, all studied proxies suggest well-developed anoxic conditions in the water
370 column, leading to much higher U and Mo accumulation rates in these sediments
371 compared to sediments surrounding S5 (Figures 2 and 3). None of the measured
372 geochemical parameters in the sediments (Fig. 2) show any sign of the hiatus proposed
373 by Cane et al. (2002) at around 87 cm (although no data are available at 88-90 cm).

374 However, the redox-sensitive proxies suggest a change from the early to the late part of
375 S5. During the early stages of sapropel formation, the RSTE proxies (Fe, U, Mo, V)
376 show a gradual increase above background values, consistent with developing anoxia.
377 Further increases during the latter part of S5 (above 94 cm) are consistent with the
378 development of increasingly euxinic conditions and higher removal rates of all the
379 measured RSTE. While the high U/Al, Mo/Al and V/Al ratios tail off slightly towards
380 the end of S5, the Fe/Al remains as high as in the sediments immediately beneath (Fig.
381 3).

382

383 The progressive increase in [Mo] and [U] during S5 is coupled with $\delta^{98}\text{Mo}_{\text{auth}}$
384 increase and $\delta^{238}\text{U}_{\text{auth}}$ decrease, suggesting progressively more quantitative uptake of
385 both elements, with U and Mo isotope compositions moving towards the seawater
386 compositions and the $\text{Mo}_{\text{EF}}/\text{U}_{\text{EF}}$ moving towards the modern seawater ratio (Fig 4).
387 There is a marked drop in $\delta^{98}\text{Mo}_{\text{auth}}$ values from the pre-sapropel sediment value of
388 around +2.4‰ at 106.5 cm depth to approximately +1.2‰ in the first sapropel sample
389 at 101.5 cm (Fig. 2). Given the corresponding increase in [Mo] from 6 to 25 ppm (Table
390 1), this drop could represent a shift from sulfidic porewater Mo uptake in the sediment
391 to dominant uptake from anoxic \pm sulfidic bottom waters. This transition could thus
392 represent the point at which mechanisms for Mo and U uptake become decoupled.

393

394 The elevated $\delta^{98}\text{Mo}_{\text{auth}}$ values (+1.2‰ to +2.3‰) within S5 are in a similar
395 range to those observed in sediments from modern euxinic basins (e.g. Black Sea,
396 Cariaco Basin, Lake Rogoznica: Arnold et al., 2004; Neubert et al., 2008, Bura-Nakić
397 et al., 2018), suggesting at least intermittent euxinic conditions in the water column that
398 allow for the molybdate to tetra-thiomolybdate transformation. The progressive

399 increase in $\delta^{98}\text{Mo}_{\text{auth}}$ from the beginning (+1.2-1.8‰) to the end (+2.0-2.3‰) of S5
400 could reflect a transition from weaker/intermittent to stronger/persistent euxinia, and
401 more quantitative Mo removal. However, the effective molybdate to tetra-
402 thiomolybdate transformation is equally affected by the time scale of transformation
403 relative to that of deep-water renewal (Dahl et al., 2010). Thus, a decrease in deep-
404 water ventilation may exert an equally important control on isotopically quantitative
405 Mo sediment uptake (e.g. Bura-Nakic et al., 2018), as observed in the later section of
406 S5. Of course, these processes are likely linked, as lower rates of inmixing of
407 oxygenated waters may increase anoxia and euxinia in the deeper water column.

408

409 The high [U] and elevated $\delta^{238}\text{U}_{\text{auth}}$ (+0.1‰ to -0.15‰) during S5 are also
410 similar to those observed in modern euxinic basins (e.g. Saanich Inlet, Black Sea,
411 Cariaco Basin, Lake Rogoznica: Weyer et al., 2008; Andersen et al., 2014; Holmden et
412 al., 2015; Bura-Nakić et al., 2018). Based on these modern analogs, the progressive
413 decrease in $\delta^{238}\text{U}_{\text{auth}}$ during S5 is indicative of permanently anoxic bottom waters and
414 steady-state diffusion-driven U removal into the reducing sediments, resulting in
415 decreasing $\delta^{238}\text{U}_{\text{auth}}$ from increasing U depletion in the bottom waters (Andersen et al.,
416 2014; Andersen et al., 2017). This U depletion is driven by the rate of U input versus
417 that of removal and, therefore, also linked to the time scales of deep-water renewal.

418

419 An alternative explanation for the evolution of the RSTE and U-Mo isotope
420 systematics during S5 could be related to an increasing addition of these elements from
421 freshwater inputs. Matthews et al. (2017) discussed this issue for sapropel S1 in the
422 Nile Fan and found that the effect of river Nile Mo input would not significantly lower
423 seawater $\delta^{98}\text{Mo}$ above core site ODP 967. Also, the authigenic enrichments are orders

424 of magnitude above potential riverine supply, and the $\text{Mo}_{\text{EF}}/\text{U}_{\text{EF}}$ ratio during most of
425 S5 is close to the modern seawater composition; these relationships would be fortuitous
426 if riverine Mo and U supplies were significant. Furthermore, Mo and U freshwater
427 input is very unlikely to concomitantly lead to waters with $\delta^{98}\text{Mo}$ values similar to
428 seawater and the highest sedimentary $\delta^{238}\text{U}$ values, unless they were highly anomalous
429 with respect to rivers measured to date (Archer & Vance, 2008; Andersen et al. 2017).
430 Thus, during S5, both U and Mo isotope systems instead respond to the time scales of
431 deep-water renewal and ventilation, despite the different removal mechanisms for Mo
432 (precipitation within an anoxic–sulfidic water column) and U (diffusion into, and
433 reduction within sulfidic sediments). This linked behavior is also indicated by the
434 roughly linear correlation between the evolution of $\delta^{238}\text{U}_{\text{auth}}$ and $\delta^{98}\text{Mo}_{\text{auth}}$ (Fig 4b).

435

436 *5.3 Estimates of U water column depletion from $\delta^{238}\text{U}$ in anoxic sediments*

437 A compilation of globally distributed semi-restricted and euxinic basins shows that
438 $\delta^{238}\text{U}_{\text{auth}}$ in the sediments exhibits a near-linear correlation with [U] depletion in basinal
439 bottom waters relative to [U] in the oxic surface waters (Fig. 5). This observation is in
440 keeping with the expectation of a linear relationship between sediment $\delta^{238}\text{U}$ and
441 bottom-water $\delta^{238}\text{U}$ and U depletion derived from a diffusion-driven model of U loss
442 into the sediments of euxinic basins with a fractionation factor of ~0.6% (see Andersen
443 et al., 2014 and Bura-Nakić et al., 2018 for details). Although other U removal
444 processes in the water column may occur (e.g. Rolison et al., 2017; Bura-Nakic et al.,
445 2018), these have been shown to be of secondary importance compared to the *in situ* U
446 reduction within sediments in euxinic basins (Bura-Nakic et al., 2018). This finding is
447 supported by the good agreement between the regression line for modern-day restricted
448 euxinic basins (Fig. 5) and that expected from the diffusion-driven U loss model

449 discussed above. In the former, the range from 0% to 100% bottom-water U loss
450 corresponds to $\delta^{238}\text{U}_{\text{auth}}$ of -0.42‰ and +0.19‰, respectively, whilst for the model this
451 range is -0.40‰ to +0.20‰. Thus, bottom-water U depletion estimates agrees to within
452 <3% when comparing these two methods.

453

454 The empirical correlation from modern-day settings can be used to quantify
455 bottom-water U depletion in the Eastern Mediterranean at 2550 m during S5, by
456 transforming $\delta^{238}\text{U}_{\text{auth}}$ sediment data to U depletion values (Fig. 5). Such an approach
457 yields estimates of bottom-water U depletion from the beginning to the end of S5 that
458 progressively increase from **12±24%** (96.5 cm) to **54±23%** (75.5 cm). The uncertainty
459 of these estimates stem from the ±2S.D. uncertainty on the coefficients of the linear
460 regression to the modern data in Fig. 5. It is important to note that the evolving bottom-
461 water U depletions during S5 that can be obtained from sedimentary $\delta^{238}\text{U}_{\text{auth}}$ are not
462 directly observable from [U] data or U/Al ratios (e.g. Fig. 3), as elemental proxies are
463 also influenced by variable local U removal fluxes and sedimentation rates.

464

465 *5.4 Using $^{238}\text{U}/^{235}\text{U}$ and deep-water renewal rates in semi-restricted anoxic basins: a* 466 *concept and a test in the Black Sea*

467 The sedimentary $\delta^{238}\text{U}_{\text{auth}}$ data can be used to provide constraints on the deep-water
468 renewal rates during the formation of S5, with the help of a conceptual model. Here, a
469 restricted basin is considered as a water column of unit area in which oxic surface and
470 near-surface waters are separated by a chemocline from anoxic/euxinic waters below.
471 The depth profile of [U] within the anoxic water column is set by the interaction
472 between U loss to sediment at the base of the water column, and re-supply of U across
473 the chemocline from U-rich oxic waters. At steady state, the total U depletion in the

474 water column (relative to the U-rich oxic waters) is a function of the U loss/resupply
475 rate. We can therefore apply our $\delta^{238}\text{U}_{\text{auth}}$ -based estimates of bottom-water U depletion
476 to calculate the rates of U resupply to the anoxic water column, i.e. the water renewal
477 timescale τ , given by:

478

$$479 \quad \tau = \frac{\Delta U}{\varphi_{\text{sed}}} \quad \text{Eqn. 1}$$

480

481 where ΔU is the total-water-column U deficit (Fig. 6) and φ_{sed} is the U loss flux to
482 sediment.

483

484 The simplest calculation of total water column U deficit is derived by assuming
485 that U transport within the sub-chemocline water column takes place only due to small-
486 scale mixing processes in the vertical direction, i.e. by turbulent diffusion. In this case,
487 the resulting [U] profile will be linear, e.g. as observed in the Rogoznica sea-lake on
488 the Croatian coast (Bura-Nakić et al., 2018), and the average U depletion over the entire
489 anoxic water column will simply be one-half of the bottom-water U depletion estimate,
490 derived from $\delta^{238}\text{U}_{\text{auth}}$ as calculated in Section 5.3. The value of ΔU can then be
491 calculated as the difference in U inventory between that expected from conservative
492 behavior of U, and the inventory calculated from the estimate of U depletion (Fig. 6):

493

$$494 \quad \Delta U = U_{\text{oxic}} \cdot L - \frac{f_{\text{bottom}}}{2} (U_{\text{oxic}} \cdot L) \quad \text{Eqn. 2}$$

495

496 where U_{oxic} is [U] in oxic surface waters above the chemocline, L is the depth of the
497 water column below the chemocline, and f_{bottom} is the fractional depletion of U at the

498 base of the water column derived from $\delta^{238}\text{U}_{\text{auth}}$. In addition to these parameters, in
499 order to estimate the water renewal timescale τ we also require independent knowledge
500 of the U loss flux to sediment φ_{sed} (Eqn. 1).

501

502 Before examining the Eastern Mediterranean during S5, we first assess this
503 simple conceptual model using data from the modern Black Sea. The value of ΔU can
504 be calculated from the known (but uncertain) parameters listed in Table 2. Additionally,
505 the U loss flux to sediment is estimated to be $100 \mu\text{g}/\text{cm}^2/\text{yr}$ (Anderson et al., 1989;
506 Andersen et al., 2014), with an uncertainty of $\pm 25 \mu\text{g}/\text{cm}^2/\text{yr}$. This U influx to sediments
507 is similar to other modern euxinic restricted basins, taking into consideration the lower
508 surface water [U] (~ 2.2 ppb) in the Black Sea relative to the open ocean [U] (~ 3.3 ppb)
509 (e.g. $\sim 150 \text{ ng}/\text{m}^2/\text{y}$ of Cariaco Basin; Andersen et al., 2014). Based on these values, we
510 calculate a deep-water renewal timescale of **830⁺⁶⁹⁰/₋₅₀₀ years** (median and 97.5/2.5
511 percentile), in good agreement with independent estimates of Black Sea deep-water
512 renewal rates (~ 400 - 1000 yr; *cf.* Algeo and Rowe, 2012). In our calculation, the
513 uncertainty is propagated numerically by a Latin Hypercube sampling procedure (10^4
514 iterations) from the uncertainties on L , f_{bottom} and the φ_{sed} (see Eqns.1, 2 and Table 2).
515 Note that any uncertainty arising from U depletion profiles that deviate from a perfect
516 linear relationship with depth (e.g Black Sea, Anderson et al., 1989; Rolison et al.,
517 2017) are implicitly incorporated into the empirical calibration regression line for
518 estimating bottom-water U depletion from the sediment $\delta^{238}\text{U}_{\text{auth}}$ given in Figure 5.

519

520 *5.5. Application to the Eastern Mediterranean during sapropel S5*

521 We make the same calculation for the ODP 967 samples in the Eastern
522 Mediterranean at the end of S5, as this is the time when our model assumptions

523 (continuous euxinia and steady state) are most likely to be fulfilled. Performing the
524 calculation for the sediment at 75.5 cm, with the lowest $\delta^{238}\text{U}_{\text{auth}}$, we obtain a deep-
525 water renewal timescale of **1030⁺⁸²⁰/₋₅₂₀ years**. The slightly increased uncertainty
526 relative to the Black Sea estimation results almost entirely from higher uncertainty on
527 the depth of the S5 anoxic chemocline, for which there are variable estimates: based on
528 benthic faunal proxies it has been suggested that anoxic (benthic azoic) conditions
529 reached up to approximately 1000 m depth (Schmiedl et al., 2003; Capotondi et al.,
530 2006), which is also approximately the saddle height between the Levantine and Ionian
531 Sea. However, euxinic conditions up to the photic zone (~200 m) have also been
532 proposed on the basis of organic biomarkers for S5 at site ODP 971 (~2000 m water
533 depth) in the central Eastern Mediterranean Sea (Rohling et al., 2006). Similarly,
534 Wegwerth et al (2018), infer water column euxinic conditions reaching up to a shallow
535 photic zone redoxcline at the termination of S5 in the Black Sea. In our calculation, the
536 chemocline is taken to be somewhere between 200 and 1400 m (800±600 m), to cover
537 the large range in published estimates (see Table 2 for parameters and uncertainties).

538

539 Doing the same calculation for sediments at 96.5 cm (with highest $\delta^{238}\text{U}_{\text{auth}}$
540 closer to the S5 initiation), with U depletions estimate of $12^{+24}/_{-12}\%$, and with the same
541 assumptions of continuous anoxia and steady state, we obtain deep-water renewal rates
542 of **340⁺³⁸⁵/₋₃₂₅ years**. Yet, a finer-grained temporal analysis of the evolution of deep-
543 water overturning rates across S5 is precluded by the uncertainties on input parameters,
544 and by time constraints for reaching steady state. However, on a quantitative level, the
545 decreasing $\delta^{238}\text{U}$ values from the start to the end of S5, coupled with $\delta^{98}\text{Mo}$ values
546 moving towards the seawater composition, clearly suggest a progressive development
547 of water mass restriction and increasing euxinia. Despite the relatively large uncertainty

548 on the calculated deep-water renewal time, our calculations suggest a very significant
549 slow-down in deep-water renewal above ODP 967 at the end of the last interglacial and
550 during S5, compared to the deep-water overturning timescales of ~100 years in the
551 modern Eastern Mediterranean (Rohling et al., 2015). Although these results are based
552 on the ODP 967 site, U and Mo respond in relation to the deep-water circulation in the
553 larger basin, thus reflecting the general systematics of the whole basin and a slowdown
554 of the entire Eastern Mediterranean overturning system.

555

556 **6. Implications for the Eastern Mediterranean during S5**

557 The Mo-U isotopes and RSTE profiles across S5 in ODP 967 are consistent with
558 development of deep-water stagnation and an anoxic chemocline with persistent
559 euxinia leading to near-quantitative sedimentary uptake of Mo and a $\delta^{98}\text{Mo}$ value close
560 to that of seawater. A similar pattern, involving the progressive move of sedimentary
561 $\delta^{98}\text{Mo}$ values towards the seawater composition at the end of the last interglacial, has
562 also been observed in the Black Sea (Wegwerth et al., 2018), suggesting a temporal
563 link to the development of euxinia in the Eastern Mediterranean at the same time. The
564 Eastern Mediterranean as a whole differs from the Black Sea in not being strongly
565 physically restricted, though this specific site, situated on the flank of the Hellenic
566 trench at the interface between the African and Eurasian plates, could be prone to more
567 localized restriction. Nevertheless, strong restriction due to a ‘bottleneck’ situation like
568 the Black Sea is an unlikely control on the development of bottom water euxinia in the
569 Eastern Mediterranean Sea. Nor is there evidence of significant Mo depletion in the
570 sapropel due to strong restriction (Fig. 4a). The observation in this study, based on the
571 U isotope systematics, that there was a ten-fold decrease in deep-water renewal time
572 relative to the modern, from ~100 to ~1000 years at the end of S5, is most consistent

573 with a marked reduction in overturning in the Eastern Mediterranean Sea. This finding
574 provides strong support for models proposing stratification of the Eastern
575 Mediterranean Sea due to massive freshwater input (predominantly the River Nile)
576 primarily related to enhanced monsoon forcing and increased westerly rainfall
577 (Rossignol Strick et al., 1982; Emeis et al., 2003; Osborne et al., 2008; Bar-Matthews,
578 2014; Rohling et al., 2015, Grant et al., 2016).

579

580 The Mo isotope and RSTE data, furthermore, point to maximum euxinic
581 conditions in the later stages of S5 development, consistent with a progressive slow-
582 down of the overturning. It is notable that Holocene sapropel S1 shows peak
583 development shortly after its initiation (Gallego-Torres et al, 2010; Azrieli-Tal et al.,
584 2014; Matthews et al., 2017), whereas for S5 the strongest euxinic conditions occur in
585 the latter part. Late-stage V/Al ratio maxima have also been noted for S5 in several
586 Eastern Mediterranean ODP sites (Gallego-Torres et al, 2010), thus reinforcing that
587 peak euxinic conditions occurred in the later stages across the whole basin. Modelling
588 studies of Grimm et al. (2015) show that rapid S1 initiation occurred at the end of a
589 long period (~6 ky) of deep-water stagnation resulting from post-deglaciation sea-level
590 rise, while Grant et al. (2016) show that monsoon run-off was the main trigger for S5
591 formation. Since S5 was deposited following a glacial termination (MIS 6), it suggests
592 that the extended period of prior deep-water stagnation modelled by Grimm et al.
593 (2015) for S1 did not occur for S5. One scenario for the late peak euxinic conditions
594 could involve a relative sea level drop from about +8 to about -20 msl (meters above
595 mean sea level) during the S5 period (Grant et al., 2012). A sea level drop across S5
596 could limit the renewal of deep-water via Bernouilli aspiration over the straits of Sicily,
597 necessary for normal circulation (Rohling et al., 2015) leading to decreasing deep-water

598 overturning rates towards the later part of S5. The reasons for the relatively rapid
599 collapse of S5 are also not clear. Gallego-Torres et al. (2010) proposed that rapid
600 sapropel collapse and re-oxygenation of the deep Levantine basin is related to deep-
601 water intrusion from the Northern Mediterranean Sea (Adriatic and Aegean seas). This
602 suggestion, combined with a sharp reduction in monsoon flooding (Rohling et al.,
603 2006), would be consistent with the view that deep-water overturn was related to the
604 dual effects of Bernoulli aspiration and deep-water renewal (Rohling et al., 2015).

605

606 Finally we note that the quantitative estimates of deep-water renewal rates and
607 estimates of euxinia in the water column for S5, based on the isotope systems of U and
608 Mo, respectively, show how these proxies may provide more qualitative information
609 on redox conditions in marine sediments than can be obtained from RSTE alone. These
610 principles are also applicable to other settings, as shown with the calculated deep-water
611 renewal rates for the Black Sea, and as such, can provide tools for further understanding
612 the mechanisms leading to the deposition of other organic-carbon rich sediments in the
613 past.

614

615 **7. Acknowledgements**

616 The research was supported by Israel Science Foundation grant 1140/12, ETH Zürich
617 and the Swiss National Science Foundation, through grant 200020_165904. Olga
618 Berlin of the Geological Survey of Israel is thanked for making the trace and major
619 element analyses. We thank the Bristol Isotope Group for the hospitality, Elvira Bura-
620 Nakić for discussions and reviews from Thomas Nägler and two anonymous reviewers
621 that helped improving a previous version of the manuscript.

622

623 **References**

624 Algeo, T.J. and Rowe, H., 2012. Paleooceanographic applications of trace-metal
625 concentration data. *Chem. Geol.*, **324**, 6-18.

626

627 Algeo, T.J., Tribovillard, N., 2009. Environmental analysis of paleooceanographic
628 systems based on molybdenum–uranium covariation. *Chem. Geol.*, **268**, 211–225.

629

630 Andersen, M.B., Stirling, C.H., Weyer, S., 2017. Uranium isotope
631 fractionation. *Reviews in Mineralogy and Geochemistry*, **82**, 799-850.

632

633 Andersen, M.B., Elliott, T., Freymuth, H., Sims, K.W., Niu, Y. and Kelley, K.A., 2015.
634 The terrestrial uranium isotope cycle. *Nature*, **517**(7534), 356-359.

635

636 Andersen, M.B. Romaniello, S., Vance, D., Little, S.H., Herdman, R. and Lyons, T.W.,
637 2014. A modern framework for the interpretation of ²³⁸U/²³⁵U in studies of ancient
638 ocean redox. *Earth Planet. Sci. Lett.*, **400**, 184-194.

639

640 Anderson, R.F., Fleischer, M.Q., LeHurray, A.P., 1989. Concentration, oxidation state,
641 and particulate flux of uranium in the Black Sea. *Geochim. Cosmochim. Acta*, **53**,
642 2215-2224.

643

644 Almogi-Labin, A., Bar-Matthews, M., Shriki, D., Kolosovsky, E., Paterne, M.,
645 Schilman, B., Matthews, A., 2009. Climatic variability during the last ~90ka of the
646 southern and northern Levantine Basin as evident from marine records and
647 speleothems. *Quat. Sci. Rev.*, **28**, 2882-2896.

648

649 Archer, C. and Vance, D., 2008. The isotopic signature of the global riverine
650 molybdenum flux and anoxia in the ancient oceans. *Nature Geoscience*, **1**, 597-600.

651

652 Arnold, G.L., Anbar, A.D., Barling, J., Lyons, T., 2004. Molybdenum isotope evidence
653 for widespread anoxia in Mid-Proterozoic oceans. *Science*, **304**, 87-90.

654

655 Azrieli-Tal, I., Matthews, A., Bar-Matthews, M., Almogi-Labin, A., Vance, D., Archer,
656 C., Teutsch, N., 2014. Evidence from molybdenum and iron isotopes and
657 molybdenum–uranium covariation for sulphidic bottom waters during Eastern
658 Mediterranean sapropel S1 formation. *Earth Planet. Sci. Lett.*, **393**, 231-242.

659

660 Bar-Matthews, M., 2014. History of water in the Middle East and North Africa. In:
661 Holland, H.D., Turekian, K.K. (Eds.), *Treatise on Geochemistry*, vol.14, second
662 edition. Elsevier, Oxford, 109–128.

663

664 Bar-Matthews, M., Ayalon, A., Kaufman, A., 2000. Timing and hydrological
665 conditions of Sapropel events in the Eastern Mediterranean, as evident from
666 speleothems, Soreq cave, Israel. *Chem. Geol.*, **169**, 145–156.

667

668 Barling, J., Arnold, G.L., Anbar, A.D., 2001. Natural mass-dependent variations in the
669 isotopic composition of molybdenum. *Earth Planet Sci. Lett.*, **193**, 447-457.

670

671 Bermin, J., Vance, D., Archer, C., Statham, P. J., 2006. The determination of the
672 isotopic composition of Cu and Zn in seawater. *Chem. Geol.*, **226**, 280–297.

673

674 Box, M.R., Krom, M.D., Cliff, R.A., Bar-Matthews, M., Almogi-Labin, A., Ayalon,
675 A., Paterne, M., 2011. Response of the Nile and its catchment to millennial-scale
676 climatic change since the LGM from Sr isotopes and major elements of East
677 Mediterranean sediments. *Quat. Sci. Rev.*, **30**, 431-442.

678

679 Bura-Nakić, E., Andersen, M.B., Archer, C., de Souza, G.F., Marguš, M., Vance, D.,
680 2018. Coupled Mo-U abundances and isotopes in a small marine euxinic basin:
681 Constraints on processes in euxinic basins. *Geochim. Cosmochim. Acta.*, **222**, 212-29.

682

683 Cane, T., Rohling, E.J., Kemp, A.E.S., Cooke, S., Pearce, R.B., 2002. High-resolution
684 stratigraphic framework for Mediterranean sapropel S5: defining temporal
685 relationships between records of Eemian climate variability. *Palaeogeogr.*
686 *Palaeoclimatol. Palaeoecol.*, **183**, 87–101

687

688 Capotondi, L., Principato, M.S., Morigi, C., Sangiorgi, F., Maffioli, P., Giunta, S.,
689 Negri, A., Corselli, C., 2006. Foraminiferal variations and stratigraphic implications to
690 the deposition of sapropel S5 in the eastern Mediterranean. *Palaeogeogr.*
691 *Palaeoclimatol. Palaeoecol.*, **235**, 48–65.

692

693 Dahl, T.W., Anbar, A.D., Gordon, G.W., Rosing, M.T., Frei, R., Canfield, D.E., 2010.
694 The behavior of molybdenum and its isotopes across the chemocline and in the
695 sediments of sulfidic Lake Cadagno, Switzerland. *Geochim. Cosmochim. Acta.*, **74**,
696 144-163.

697

698 de Lange, G.J., Thomson, J., Reitz, A., Slomp, C.P., Speranza Principato, M., Erba, E.,
699 Corselli, C., 2008. Synchronous basin-wide formation and redox-controlled
700 preservation of a Mediterranean sapropel. *Nature Geoscience*, **1**, 606–610.

701

702 Emeis, K.C., Sakamoto, T., Wehausen, R., Brumsack, H.J., 2000. The sapropel record
703 of the eastern Mediterranean Sea—results of Ocean Drilling Program Leg 160.
704 *Palaeogeog. Palaeoclimat. Palaeoecol.*, **158**, 371-395.

705

706 Emeis, K.C., Schulz, H.M., Struck, U., Sakamoto, T., Dose, H., Erlenkeuser, H.,
707 Howell, m., Kroon, D., Paterne, M., 1998. Stable isotope and alkenone temperature
708 records of sapropels from sites 964 and 967: constraining the physical environment of
709 sapropel formation in the eastern Mediterranean sea. In: Robertson, A.H.F., Emeis,
710 K.C., Richter, C., Camerlenghi, A., Editors, *Proceedings of the Ocean Drilling
711 Program, Scientific Results*, **160**, 309-331

712

713 Gallego-Torres, D., Martinez-Ruiz, F., de Lange, G. J., Jimenez-Espejo, F.J. Ortega-
714 Huertas, M., 2010. Trace-elemental derived paleoceanographic and paleoclimatic
715 conditions for Pleistocene Eastern Mediterranean sapropels. *Palaeogeog.
716 Palaeoclimat., Palaeoecol.*, **293**, 76–89.

717

718 Goldberg, T., Archer, C., Vance, D., Poulton, S.W., 2009. Mo isotope fractionation
719 during adsorption to Fe (oxyhydr)oxides. *Geochim. Cosmochim. Acta*, **73**, 6502–6516.

720

721 Grant, K.M., Rohling, E.J., Bar-Matthews, M., Ayalon, A., Medina-Elizalde, M.,
722 Ramsey, C.B., Satow, C. and Roberts, A.P., 2012. Rapid coupling between ice volume
723 and polar temperature over the past 150,000 years. *Nature*, **491**(7426), p.744.
724

725 Grant, K.M., Grimm, R., Mikolajewicz, U., Marion, G., Ziegler, M., Rohling E.J., 2016.
726 The timing of Mediterranean sapropel deposition relative to insolation, sea-level and
727 African monsoon changes, *Quat. Sci Rev*, **140**, 125-141
728

729 Grimm, R., Maier-Reimer, E., Mikolajewicz, U., Schmiedl, G., Muller-Navarra, K.,
730 Adloff, F., Grant, K.M., Ziegler, M., Lourens, L.J., Emeis, K.C., 2016. Late glacial
731 initiation of Holocene eastern Mediterranean sapropel formation. *Nat. Commun.*, DOI:
732 10.1038/ncomms8099.
733

734 Holmden, C., Amini, M., Francois, R., 2015. Uranium isotope fractionation in Saanich
735 Inlet: A modern analog study of a paleoredox tracer. *Geochim. Cosmochim. Acta*, **153**,
736 202-215.
737

738 Johnson, J., and Steven, I., 2000. A fine resolution model of the eastern North Atlantic,
739 between the Azores, the Canary islands, and the Gibraltar Strait. *Deep Sea Res. Part I*,
740 **47**, 877-899.
741

742 Kendall, B., Dahl, T.W. and Anbar, A.D., 2017. The stable isotope geochemistry of
743 molybdenum. *Reviews in Mineralogy and Geochemistry*, **82**(1), 683-732.
744

745 Kendall, B., Komiya, T., Lyons, T.W., Bates, S.M., Gordon, G.W., Romaniello, S.J.,
746 Jiang, G., Creaser, R.A., Xiao, S., McFadden, K. and Sawaki, Y, 2015. Uranium and
747 molybdenum isotope evidence for an episode of widespread ocean oxygenation during
748 the late Ediacaran Period. *Geochim. Cosmochim. Acta*, **156**, 173-193.

749

750 Kerl, C.F., Lohmayer, R., Bura-Nakić, E., Vance, D., Planer-Friedrich, B., 2017
751 Experimental confirmation of isotope fractionation in thiomolybdates using ion
752 chromatography and detection by multi-collector ICP-MS. *Anal. Chem.*, **89**, 3123-3129
753

754 Lovley, D.R., Phillips, E.J., Gorby, Y.A. and Landa, E.R., 1991. Microbial reduction
755 of uranium. *Nature*, **350**(6317), 413-416

756

757 Malanotte-Rizzoli, P., Bergamasco, A., 1989. The circulation of the eastern
758 Mediterranean. Part 1. *Oceanologica Acta*, **12**(4), 335-351.

759

760 Matthews, A., Azrieli-Tal, I., Benkovitz, A., Bar-Matthews, M., Vance, D., Poulton,
761 S.W., Teutsch, N., Almogi-Labin, A., Archer, C., 2017. Anoxic development of
762 sapropel S1 in the Nile Fan inferred from redox sensitive proxies, Fe speciation, Fe and
763 Mo isotopes. *Chem. Geol.*, **475**, 24-39.

764

765 McManus, J., Berelson, W.B., Severmann, S., Poulson, R.I., Hammond, D.E.,
766 Klinkhammer, G.P., Holm, C., 2006. Molybdenum and uranium geochemistry in
767 continental margin sediments: paleoproxy potential. *Geochim. Cosmochim. Acta*, **70**,
768 4643-4662

769

770 Meyer, K.L., Kump, L.R., 2008. Oceanic euxinia in earth history: causes and
771 consequences. *Annu. Rev. Earth Planet. Sci.*, **36**, 251–288.
772

773 Montoya-Pino, C., Weyer, S., Anbar, A.D., Pross, J., Oschmann, W., van de
774 Schootbruuge, B., Arz, H.W., 2010. Global enhancement of ocean anoxia during Anoxic
775 Oceanic Event 2: A quantitative approach using U isotopes. *Geology* **38**, 315-318.
776

777 Neubert, N., Nägler, T.F., Böttcher, M.E., 2008. Sulfidity controls molybdenum isotope
778 fractionation in euxinic sediments: evidence from the modern Black Sea. *Geology* **36**,
779 775–778.
780

781 Nägler, T.F., Neubert, N., Böttcher, M.E., Dellwig, O., Schmetger, B., 2011. Mo isotope
782 fractionation in pelagic euxinia: results from the modern Black and Baltic Seas. *Chem.*
783 *Geol.*, **289**, 1–11.
784

785 Nägler, T.F., Anbar, A.D., Archer, C., Goldberg, T., Gordon, G.W., Greber, N.D.,
786 Siebert, C., Sohrin, Y., Vance, D., 2014. Proposal for an international molybdenum
787 isotope measurement standard and data representation. *Geostand. Geoanal. Res.*, **38**,
788 149-151.
789

790 Noordmann, J., Weyer, S., Montoya-Pino, C., Dellwig, O., Neubert, N., Eckert, S.,
791 2015. Uranium and molybdenum isotope systematics in modern euxinic basins: Case
792 studies from the central Baltic Sea and the Kyllaren fjord (Norway). *Chem. Geol.*, **396**,
793 182-195.
794

795 Osborne, A.H., Vance, D., Rohling, E.J., Barton, N., Rogerson, M., Felloon, N., 2008.
796 A humid corridor across the Shara for the migration of early modern humans out of
797 Africa, 120,000 years ago. *Proc.Natl. Acad. Sci. USA*, **105**, 16444-16447.
798
799
800 Pinardi, N., and Masetti, E., 2000. Variability of the large scale general circulation of
801 the Mediterranean Sea from observations and modelling: a review. *Palaeogeog.*
802 *Palaeoclimat. Palaeoecol.*, **158**, 153–173.
803
804 Poulson-Brucker, R.L., McManus, J., Poulton, S.W., 2012. Molybdenum isotope
805 fractionation observed under anoxic experimental conditions. *Geochem. J.*, **46**, 201-
806 209.
807
808 Poulson-Brucker, R.L., McManus, J., Severmann, S., Berelson, W.M., 2009.
809 Molybdenum behavior during early diagenesis: Insights from Mo isotopes. *Geochem.*
810 *Geophys., Geosyst.*, **10**(6).
811
812 Rogerson, M., Rohling, E.J., Bigg, G.R., Ramirez, J., 2012. Palaeoceanography of the
813 Atlantic-Mediterranean Exchange: overview and first quantitative assessment of
814 climatic forcing. *Rev. Geophys.* **50**, RG2003.
815 <http://dx.doi.org/10.1029/2011RG000376>.
816
817 Rohling, E.J., Hilgen, F.J., 1991. The eastern Mediterranean climate at times of
818 sapropel formation: a review. *Geologie en Mijnbouw*, **70**, 253-264.
819

820 Rohling, E.J., Hopmans, E.C., Sinninghe-Damsté, J.S., 2006. Water column dynamics
821 during the last interglacial anoxic event in the Mediterranean (sapropel S5).
822 *Paleoceanography* **21**, PA2018. <http://dx.doi.org/10.1029/2005PA001237>.
823

824 Rohling, E.J., Marino, G., Grant, K.M., 2015. Mediterranean climate and
825 oceanography, and the periodic development of anoxic events (sapropels). *Earth-Sci.*
826 *Rev.*, **143**, 62–97.
827

828 Rolison, J.M., Stirling, C.H., Middag, R., Rijkenberg, M. J.A., 2017. Uranium stable
829 isotope fractionation in the Black Sea: modern calibration of the $^{238}\text{U}/^{235}\text{U}$ paleo-redox
830 proxy. *Geochim. Cosmochim. Acta*, **203**, 69-88.
831

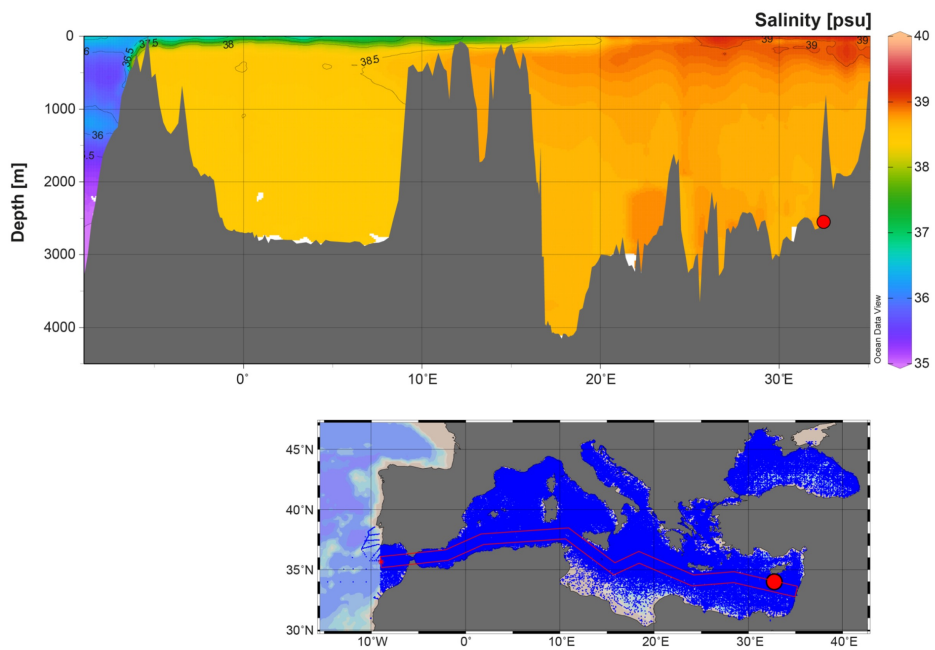
832 Rossignol-Strick, M., 1985. Mediterranean Quaternary sapropels: an immediate
833 response to of the African Monsoon to variation of insolation. *Paleogeog.*
834 *,Paleoclimatol. , Paleoecol.*, **49**, 237–265.
835

836 Rossignol-Strick, M., Nesteroff, V., Olive, P., Vergnaud-Grazzini, C., 1982. After the
837 deluge: Mediterranean stagnation and sapropel formation. *Nature*, **295**, 105-110.
838

839 Scheiderich, K., Zerkle, A.L., Helz, G.R., Farquhar, J., Walker, R.J., 2010.
840 Molybdenum isotope, multiple sulfur isotope, and redox sensitive element behavior in
841 early Pleistocene Mediterranean Sapropels. *Chem. Geol.*, **279**, 134-144.
842

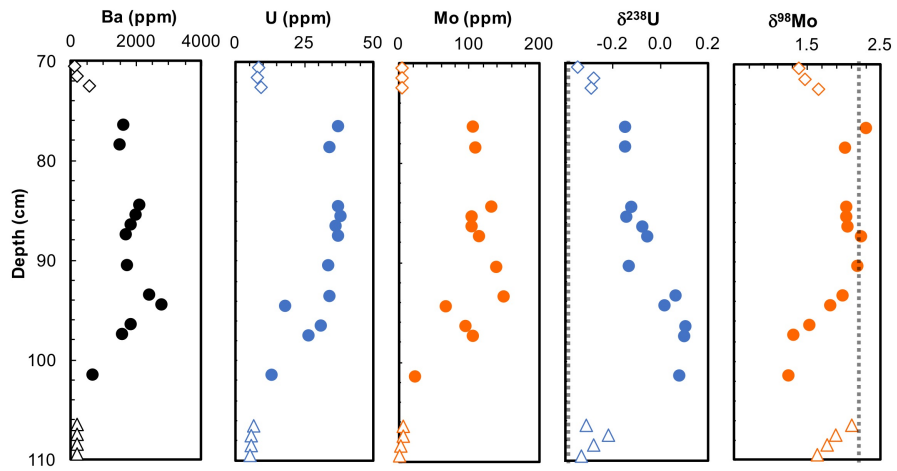
843 Schmiedl, G., Mitschele, A., Beck, S., Emeis, K.C., Hemleben, Ch., Schultz, H.,
844 Sperling, M., Weldeab, S., 2003. Benthic foraminiferal record of ecosystem variability

845 in the eastern Mediterranean Sea during times of sapropel S5 and S6 deposition.
846 *Palaeogeogr. Palaeoclimatol. Palaeoecol.*, **190**, 139-164.
847
848 Scrivner, A., Vance, D., Rohling, E.J., 2004. New neodymium isotope data quantify
849 Nile involvement in Mediterranean anoxic episodes. *Geology*, **32**, 565–568.
850
851 Siebert, C., Nägler, T.F., Kramers, J.D., 2001. Determination of molybdenum isotope
852 fractionation by double-spike multicollector inductively coupled plasma mass
853 spectrometry. *Geochem. Geophys. Geosyst.*, **2**, 2000GC00124
854
855 Stirling, C.H., Andersen, M.B., Potter, E.-K., Halliday, A.N., 2007. Low temperature
856 Isotope Fractionation of uranium. *Earth Planet. Sci. Lett.*, **264**, 208-225.
857
858 Thomson, J., Mercone, D., de Lange, G.J., van Santvoort, P.J.M., 1999. Review of
859 recent advances in the interpretation of Eastern Mediterranean sapropel S1 from
860 geochemical evidence. *Marine Geol.*, **153**, 77–89.
861
862 Wegwerth, A., Eckert, S., Dellwig, O., Schnetger, B., Severmann, S., Weyer, S.,
863 Brüske, A., Kaiser, J., Köster, J., Arz, H.W. and Brumsack, H.J., 2018. Redox evolution
864 during Eemian and Holocene sapropel formation in the Black Sea. *Palaeogeog.*
865 *Palaeoclimatol. Palaeoecol.*, **489**, 249-260.
866
867 Weyer, S., Anbar, A.D., Gerdes, A., Gordon, G.W., Algeo, T.J., Boyle, E.A., 2008.
868 Natural fractionation of $^{238}\text{U}/^{235}\text{U}$. *Geochim. Cosmochim. Acta*, **72**, 345-359.
869



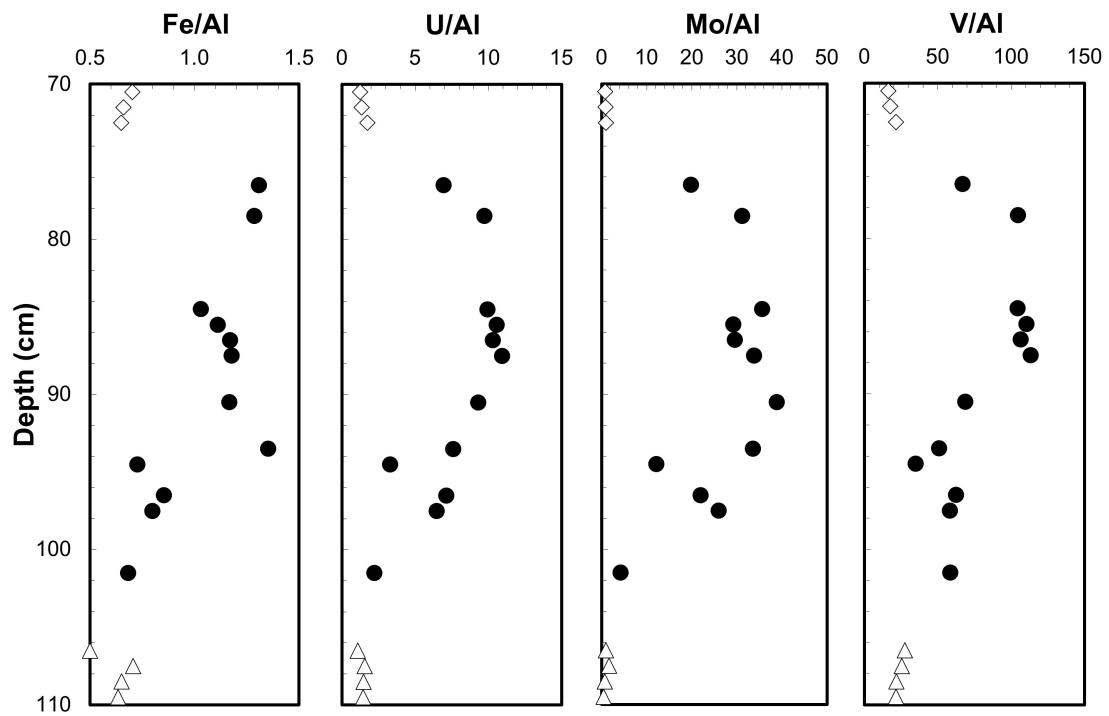
870

871 Figure 1. Vertical salinity profile (top) through the Mediterranean basin (bottom). The
 872 position of the studied core ODP 967 is marked with the red dot. Generated in Ocean
 873 Data View (<https://odv.awi.de>).



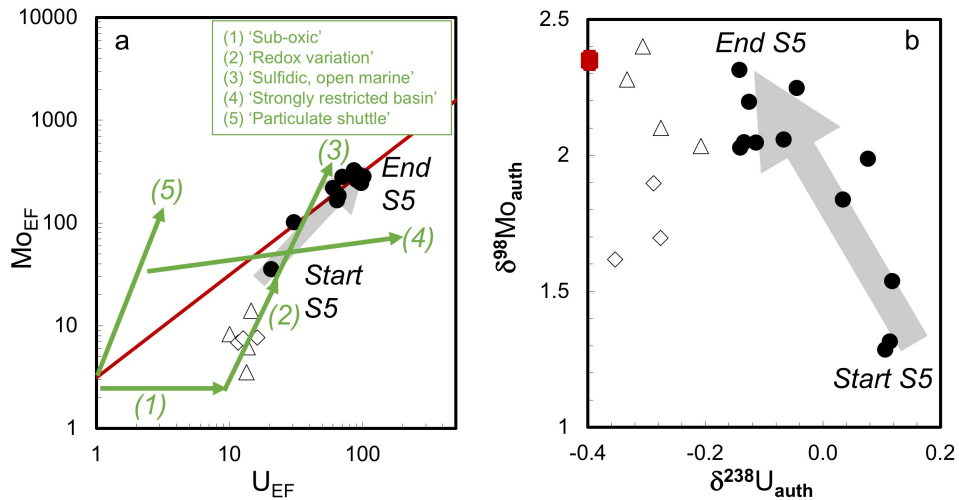
874

875 Figure 2. Core 967C-H5; depth in cm (110-70cm) vs. [Ba], [Mo], [U], $\delta^{98}\text{Mo}$, $\delta^{238}\text{U}$
 876 for post-S5 (open diamonds), S5 (filled circle) and pre-S5 (open triangles) samples. The
 877 open ocean isotope composition is shown as a dotted line for $\delta^{98}\text{Mo}$ (+2.34‰) and for
 878 $\delta^{238}\text{U}$ (-0.39‰) - the latter at the far left, close to the y-axis.



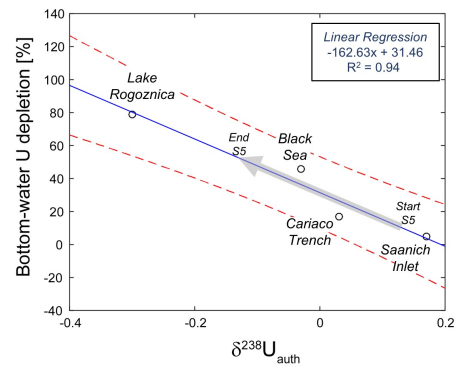
879

880 Figure 3. Ratios of Fe, U, Mo and V (ppm) vs Al (wt%), symbols as in Figure 2, show
 881 elevated values during S5 compared to before and after S5. All element to Al ratios also
 882 shows a general increase during S5. Although the last measured S5 sample at 76.5cm
 883 has as high Fe/Al as the previous sample, U/Al, Mo/Al and V/Al have all decreased.



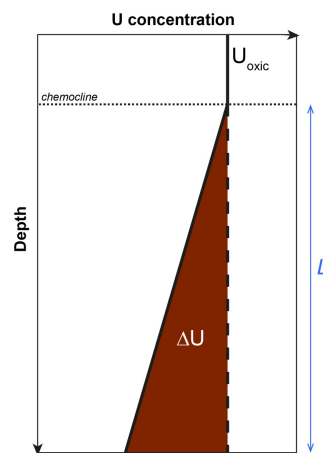
884

885 Figure 4. Cross-plots of authigenic U and Mo and their isotope systematics (symbols
 886 as in Figure 2). (a) The bold red line in (a) shows the Mo/U ratio in modern seawater.
 887 The green arrows show schematic evolution in enrichment factor trajectories based on
 888 physical and chemical controls on water masses, as presented by Algeo & Tribovillard
 889 (2009). The filled red symbol in (b) shows $\delta^{238}U$ and $\delta^{98}Mo$ compositions of modern
 890 open ocean seawater. Grey arrow shows evolution from beginning to end of S5. Linear
 891 regression through the S5 data gives $y = -2.65x + 1.84$ with $R^2 = 0.68$.



892

893 Figure 5. Cross-plot and linear regression (solid line, dashed lines are $2\sigma_{SD}$ uncertainty
 894 envelope) of authigenic $\delta^{238}U$ vs. bottom-water [U] depletion compared to the oxic
 895 surface (in percent) for a range of modern euxinic basins (Data are taken from Bura-
 896 Nakić et al., 2018, see this paper for data references). Note that data from Kyllaren
 897 Fjord (Noordmann et al., 2015), also reported in Bura-Nakić et al. (2018), has been left
 898 out from this calibration, since this site is affected by unusually high H_2S due to recent
 899 restriction of the fjord due to human activities. Grey arrow along the linear regression
 900 line shows the evolution of $\delta^{238}U_{auth}$ from the start to end of S5 (Fig. 1). Bottom-water
 901 U depletion above euxinic sediment samples can be calculated using the measured
 902 $\delta^{238}U_{auth}$ and the linear regression equation; $U_{depletion} (\%) = 162.63 * \delta^{238}U_{auth} + 31.46$.



903
 904 Figure 6. Schematic illustration of the creation of a water column U depletion profile
 905 (solid line) in a restricted basin with oxic surface waters separated from more stagnant
 906 anoxic/euxinic waters at depth. The total loss of U (ΔU) below the chemocline

907 compared to conservative U behavior (dashed line) can be calculated with knowledge
908 of the length-scale of the water column below the chemocline (L), the [U] of the oxic
909 surface waters above the chemocline (U_{oxic}) and the degree of U depletion at the base
910 of the water column.
911

Table 1
Selected concentrations and isotope compositions for ODP 967C 1H-5, 2550 m depth¹

ID cm	U ppm ²	Mo ppm ²	V ppm ²	Ba ppm ²	Al wt% ²	Ca wt% ²	Fe wt% ²	$\delta^{238}\text{U}$ ‰ ³	$\delta^{98}\text{Mo}$ ‰ ⁴	U_{auth} ppm ⁵	Mo_{auth} ppm ⁶	$\delta^{238}\text{U}_{\text{auth}}$ ‰ ⁷	$\delta^{98}\text{Mo}_{\text{auth}}$ ‰ ⁸
70-1	8.0	5.2	105	130	6.4	6.0	4.5	-0.35±3	1.38±3	7.1	4.4	-0.35±4	1.62±4
71-2	7.8	5.1	100	177	5.7	4.1	3.8	-0.28±3	1.47±3	7.0	4.4	-0.28±4	1.70±4
72-3	9.2	4.8	113	550	5.2	3.7	3.4	-0.29±3	1.65±3	8.5	4.2	-0.29±4	1.90±4
76-7	37	107	361	1631	5.4	3.9	7.0	-0.15±3	2.30±3	37	106	-0.14±3	2.31±3
78-9	34	109	366	1500	3.5	10	4.5	-0.15±3	2.02±3	33	109	-0.14±3	2.03±3
84-5	37	133	390	2102	3.7	2.7	3.9	-0.12±3	2.04±3	37	133	-0.11±3	2.05±3
85-6	38	105	397	2000	3.6	11	4.0	-0.14±3	2.04±3	37	105	-0.13±3	2.05±3
86-7	36	104	373	1838	3.5	2.5	4.1	-0.07±3	2.05±3	36	103	-0.07±3	2.06±3
87-8	37	115	385	1700	3.4	10	4.0	-0.05±3	2.24±3	37	115	-0.04±3	2.25±3
90-1	34	140	247	1750	3.6	9.8	4.2	-0.13±3	2.19±3	33	140	-0.13±3	2.20±3
93-4	34	150	228	2409	4.5	3.2	6.1	0.07±3	1.98±3	33	150	0.08±3	1.99±3
94-5	18	67	194	2800	5.5	4.0	4.0	0.02±3	1.82±3	17	66	0.03±3	1.84±3
96-7	31	95	271	1867	4.3	3.1	3.7	0.11±3	1.53±3	30	95	0.12±3	1.54±3
97-8	27	107	240	1576	4.1	2.9	3.3	0.11±3	1.31±3	26	106	0.11±3	1.32±3
101-2	13	25	341	677	5.8	4.2	4.0	0.08±3	1.25±3	12	24	0.11±3	1.29±3
106-7	6.5	6.0	166	188	6.0	8.0	3.0	-0.31±3	2.11±3	5.6	5.2	-0.31±3	2.40±4
107-8	5.3	5.7	86	176	3.4	2.4	2.4	-0.22±3	1.89±3	4.9	5.3	-0.21±3	2.03±3
108-9	5.4	2.7	79	180	3.6	2.6	2.4	-0.28±3	1.76±3	4.6	2.2	-0.28±3	2.10±4
109-0	5.0	1.4	74	185	3.5	2.5	2.2	-0.33±3	1.63±3	4.6	1.0	-0.33±3	2.28±6

¹ See supplementary table for further details.

² Errors (RSD) on single values for major and trace elements are ±5%.

³ $\delta^{238}\text{U}$ values normalised to the CRM-145 uranium standard and errors are 2SD and refer to last digit

⁴ $\delta^{98}\text{Mo}$ values normalised to NIST SRM 3134 = 0.25‰ and errors are 2SD and refer to last digit.

⁵ Authigenic fraction obtained subtracting detrital contribution using U/Al of 10.8×10^{-6} g/g and biogenic carbonate contribution of 3.25×10^{-6} g/g (see suppl. Table for relative fractions).

⁶ Authigenic fraction obtained subtracting detrital contribution using Mo/Al of 11.9×10^{-6} g/g (see suppl. Table for relative fractions).

⁷ Authigenic $\delta^{238}\text{U}$ values obtained subtracting detrital and carbonate contribution calculated in (5) and detrital $\delta^{238}\text{U}$ of -0.3‰ and biogenic carbonate $\delta^{238}\text{U}$ of -0.4‰. Uncertainty estimate for the reduced authigenic $\delta^{238}\text{U} = \text{error}(\delta^{238}\text{U}_{(\text{measured})} * (\delta^{238}\text{U}_{(\text{reduced})} - \delta^{238}\text{U}_{(\text{detrital})}) / (\delta^{238}\text{U}_{(\text{measured})} - \delta^{238}\text{U}_{(\text{detrital})}) * (1/\text{reduced}_{(\text{fraction})})$.

⁸ Authigenic $\delta^{98}\text{Mo}$ values obtained subtracting detrital and carbonate contribution calculated in (6) and detrital $\delta^{98}\text{Mo}$ of 0‰. Uncertainty estimate for the reduced authigenic $\delta^{98}\text{Mo} = \text{error}(\delta^{98}\text{Mo}_{(\text{measured})} * (\delta^{98}\text{Mo}_{(\text{reduced})} - \delta^{98}\text{Mo}_{(\text{detrital})}) / (\delta^{98}\text{Mo}_{(\text{measured})} - \delta^{98}\text{Mo}_{(\text{detrital})}) * (1/\text{reduced}_{(\text{fraction})})$.

912

Table 2

Parameters used for calculating deep-water renewal timescales from U depletion

	<i>Black Sea</i>	<i>E. Med. end S5</i>
<u>U depletion estimates:</u>		
bottom-water depletion:	$\% = 162.63 * \delta^{238}\text{U}_{\text{auth}} + 31.46$	
$\delta^{238}\text{U}_{\text{auth}}$ (‰)	0±0.03	-0.15±0.03
Bottom-water U depletion (%) f_{bottom}	36±22	54±23
<u>Water column properties:</u>		
Basin depth (km)	2.3	2.6
Chemocline depth (km)	0.2±0.1	0.8±0.6
Water column below chemocline (km) L	2.1±0.1	1.8±0.6
<u>Water-column U depletion estimates:</u>		
Initial [U] in surface waters (ppb) U_{avia}	2.2±0.1	3.3±0.3
Expected U in 1D sub-chem. water column (ng)	4.62x10 ⁹	5.94x10 ⁹
U deficit in 1D water column (ng) ΔU	6.93x10 ⁸	8.91x10 ⁸
<u>Uranium flux into sediments:</u>		
U loss flux (ng/cm ² /y)	100±25	150±25
U loss per 1m ² sediment (ng/yr) ϕ_{sed}	1x10 ⁶	1.5x10 ⁶
Water renewal timescale $\tau = \Delta U / \phi_{\text{sed}}$	830 ⁺⁶⁹⁰ / ₋₅₀₀	1030 ⁺⁸²⁰ / ₋₅₂₀